Naval Research Laboratory
Washington, DC 20375-5320

NRL/8225/MR—2022/1

A Discontinuous Galerkin Method for Ideal Magnetohydrodynamics in NRL's JENRE® Code

CHRISTIAN L. BACHMAN

Space Mechanical Systems Development Branch
Spacecraft Engineering Division

ANDREW D. KERCHER

Laboratories for Computational Physics and Fluid Dynamics
Materials Science and Component Technology Directorate

March 29, 2022

REPORT DOCUMENTATION PAGE

Form Approved
OMB No. 0704-0188

1. REPORT DATE *(DD-MM-YYYY)*	**2. REPORT TYPE**	**3. DATES COVERED** *(From - To)*
29-03-2022	NRL Memorandum Report	04-26-2020 – 04-25-2022

4. TITLE AND SUBTITLE

A Discontinuous Galerkin Method for Ideal Magnetohydrodynamics in NRL's JENRE® Code

5a. CONTRACT NUMBER

5b. GRANT NUMBER

5c. PROGRAM ELEMENT NUMBER
NISE

6. AUTHOR(S)

Christian L. Bachman and Andrew D. Kercher

5d. PROJECT NUMBER

5e. TASK NUMBER

5f. WORK UNIT NUMBER
N2W6

7. PERFORMING ORGANIZATION NAME(S) AND ADDRESS(ES)

Naval Research Laboratory
4555 Overlook Avenue, SW
Washington, DC 20375-5320

8. PERFORMING ORGANIZATION REPORT NUMBER

NRL/8225/MR--2022/1

9. SPONSORING / MONITORING AGENCY NAME(S) AND ADDRESS(ES)

Naval Research Laboratory
4555 Overlook Avenue, SW
Washington, DC 20375-5320

10. SPONSOR / MONITOR'S ACRONYM(S)

NRL-NISE

11. SPONSOR / MONITOR'S REPORT NUMBER(S)

12. DISTRIBUTION / AVAILABILITY STATEMENT

DISTRIBUTION STATEMENT A: Approved for public release; distribution is unlimited.

13. SUPPLEMENTARY NOTES

Karles Fellowship

14. ABSTRACT

We outline progress made towards the development of a computational model coupling electromagnetic effects with fluid dynamics for use in the study of ionized flows around hypersonic vehicles. The initial progress takes the form of the complete implementation of an ideal magnetohydrodynamics (MHD) solver in NRL's JENRE® multiphysics code. This lays the important groundwork for the implementation of more detailed and realistic modeling capabilities. We outline the numerical methods, implementation, and successful validation of the ideal MHD model in the unstructured computational mesh framework of JENRE®, which is novel in the field of MHD and will play a critical role in modeling realistic hypersonic vehicle geometries in the future.

15. SUBJECT TERMS

16. SECURITY CLASSIFICATION OF:			**17. LIMITATION OF ABSTRACT**	**18. NUMBER OF PAGES**	**19a. NAME OF RESPONSIBLE PERSON**
					Christian Bachman
a. REPORT	**b. ABSTRACT**	**c. THIS PAGE**	U	27	**19b. TELEPHONE NUMBER** *(include area code)*
U	U	U			(202) 767-8573

This page intentionally left blank.

CONTENTS

FIGURES

TABLES

This page intentionally left blank

EXECUTIVE SUMMARY

We outline progress made towards the development of a computational model coupling electromagnetic effects with fluid dynamics for use in the study of ionized flows around hypersonic vehicles. The initial progress takes the form of the complete implementation of an ideal magnetohydrodynamics (MHD) solver in NRL's JENRE® Multiphysics Code. This lays the important groundwork for the implementation of more detailed and realistic modeling capabilities. We outline the numerical methods, implementation, and successful validation of the ideal MHD model in the unstructured computational mesh framework of the JENRE® Code, which is novel in the field of MHD and will play a critical role in modeling realistic hypersonic vehicle geometries in the future

This page intentionally left blank

A DISCONTINUOUS GALERKIN METHOD FOR IDEAL MAGNETOHYDRODYNAMICS IN NRL'S JENRE® CODE

1. INTRODUCTION

Hypersonic regimes in Earth's atmosphere are often characterized by the presence of a partially ionized flow forming a plasma sheath around the vehicle. Hypersonic boost-glide and reentry vehicles can have flight Mach numbers ranging anywhere from 5 to 25, corresponding to highly varying plasma dynamics and characteristics, such as electron density, temperature, and ionization fraction. These plasma parameters play an important role in leading-edge heat flux, radio communication blackout, and increased radar cross-section [1–3]. Given the electromagnetic nature of these adverse effects, applied magnetic or electric fields can have a significant impact on mitigating them. This has become a promising area of research in the hypersonics community.

It is difficult to achieve flight enthalpies, and therefore realistic plasma chemistry, in an experimental facility, while available flight test data is also limited and often dated [4], although being pursued more in recent years [5]. For these reasons, numerical modeling remains the best method for studying plasmas within hypersonic flows and their interaction with electromagnetic fields. This motivates the implementation of a magnetohydrodynamics (MHD) solver coupled with the fluid dynamics equations. We aim to do this in NRL's existing fluid dynamic code, the JENRE® Multiphysics Framework.

The computational modeling of plasma as a continuum fluid through MHD has been studied for many years, primarly in an astrophysical context [6], in which the plasma is extremely hot, highly or fully ionized, and the magnetic field convects with the motion of the fluid. This is represented by the ideal MHD equations, which are analogous to the compressible Euler equations in fluid dynamics. The simplicity of ideal MHD, and the relevance of the necessary numerical techniques to more detailed models, makes ideal MHD the proper starting point for implementing an MHD solver.

In this paper we outline the implementation of ideal MHD in the JENRE® Multiphysics Framework. The set of equations are presented as a coupling of the Euler equations with Maxwell's equations for electromagnetism. We define the discontinuous Galerkin (DG) fomulation and discretization of the equations while highlighting the major developments specific to the present model. We then present the numerical results from benchmark cases, validating the implementation. Lastly, we discuss the next steps that will be taken in order to achieve the ultimate goal of developing a numerical model that fully couples electromagnetism with fluid dynamics to model ionized flows in hypersonic regimes.

2. IDEAL MAGNETOHYDRODYNAMICS EQUATIONS

2.1 General derivation

To derive the ideal MHD equations we start with the Euler equations for an inviscid, inert fluid and Maxwell's equations for electromagnetism. The two are linked through source terms representing the interaction of an electrically conducting fluid with electromagnetic fields.

Manuscript approved March 14, 2022.

$$\frac{\partial \rho}{\partial t} + \nabla \cdot (\rho \boldsymbol{v}) = 0 \tag{1}$$

$$\frac{(\partial \rho \boldsymbol{v})}{\partial t} + \nabla \cdot (\rho \boldsymbol{v}\boldsymbol{v} + P\boldsymbol{I}) = \boldsymbol{J} \times \boldsymbol{B} \tag{2}$$

$$\frac{\partial \left(\rho(E + \frac{v^2}{2})\right)}{\partial t} + \nabla \cdot \left(\left(\rho \left(E + \frac{v^2}{2}\right) + P\right)\boldsymbol{v}\right) = \boldsymbol{E} \cdot \boldsymbol{J} \tag{3}$$

$$\nabla \cdot \boldsymbol{E} = \frac{\rho_c}{\epsilon_0} \tag{4}$$

$$\nabla \cdot \boldsymbol{B} = 0 \tag{5}$$

$$\nabla \times \boldsymbol{E} = -\frac{\partial \boldsymbol{B}}{\partial t} \tag{6}$$

$$\nabla \times \boldsymbol{B} = \mu_0 \left(\boldsymbol{J} + \epsilon_0 \frac{\partial \boldsymbol{E}}{\partial t}\right) \tag{7}$$

These source terms correspond to the lorentz force in the momentum equation and the work done by the electric and magnetic fields on the fluid in the energy equation. We link the sets of equations further with the generalized Ohm's law:

$$\boldsymbol{E} + \boldsymbol{v} \times \boldsymbol{B} = \eta \boldsymbol{J}. \tag{8}$$

In the case of ideal MHD, the plasma is assumed to be infinitely conductive. Therefore, the resistivity, η, (the inverse of the conductivity) vanishes and Eq. (8) instead becomes the ideal generalized Ohm's law.

For MHD formulations we assume the modeled time scale is much greater than the time scale of the variation of the electric field; therefore, the displacement current on the right hand side of Ampere's law, Eq. (7), is approximately zero. This results in the elimination of electromagnetic wave propagation in the system and equates the current density, $\boldsymbol{J}$, to the curl of the magnetic field, normalized by the permeability of free space, μ_0.

Using Eq. (7) in the momentum source term,

$$\boldsymbol{J} \times \boldsymbol{B} = \frac{1}{\mu_0}(\nabla \times \boldsymbol{B}) \times \boldsymbol{B} = \nabla \cdot \left(\frac{1}{\mu_0}(\boldsymbol{B}\boldsymbol{B} - \frac{B^2}{2}\boldsymbol{I})\right). \tag{9}$$

Thus, the lorentz force can be added to the momentum flux as an additional term dependent only on the local magnetic field.

To handle the energy source term we first take the dot product of Eqs. (6) – (7) with $\boldsymbol{B}/\mu_0$ and $\boldsymbol{E}$, respectively, and subtract the two, giving,

$$\boldsymbol{E}\cdot\boldsymbol{J}+\frac{1}{\mu_0}\boldsymbol{B}\cdot\frac{\partial\boldsymbol{B}}{\partial t}=\boldsymbol{E}\cdot(\nabla\times\boldsymbol{H})-\frac{1}{\mu_0}\boldsymbol{B}\cdot(\nabla\times\boldsymbol{E}), \tag{10}$$

which can be rewritten and rearranged to give,

$$\boldsymbol{E}\cdot\boldsymbol{J}=-\frac{\partial}{\partial t}\left(\frac{B^2}{2\mu}\right)-\nabla\cdot(\frac{1}{\mu_0}\boldsymbol{E}\times\boldsymbol{B}), \tag{11}$$

where

$$\frac{1}{\mu_0}\boldsymbol{E}\times\boldsymbol{B}=\frac{1}{\mu_0}(\boldsymbol{v}\times\boldsymbol{B})\times\boldsymbol{B}=\frac{1}{\mu_0}\left((\boldsymbol{B}\cdot\boldsymbol{B})\boldsymbol{v}-(\boldsymbol{v}\cdot\boldsymbol{B})\boldsymbol{B}\right). \tag{12}$$

From Eq. (11) we conclude that a magnetic pressure, $B^2/(2\mu_0)$ can be added to the conserved energy density, and a new term can be added to the energy flux that is dependent on the magnetic field.

Lastly, the induction equation, Eq. (6), is expanded into a conversative-flux form using Ohm's law,

$$\frac{\partial\boldsymbol{B}}{\partial t}=-\nabla\times\boldsymbol{E}=\nabla\times(\boldsymbol{v}\times\boldsymbol{B})=\nabla\cdot(\boldsymbol{v}\boldsymbol{B}-\boldsymbol{B}\boldsymbol{v}). \tag{13}$$

Substituting the expanded electromagnetic source terms, and including the induction equation, results in the full set of ideal MHD equations:

$$\frac{\partial\rho}{\partial t}+\nabla\cdot(\rho\boldsymbol{v})=0 \tag{14}$$

$$\frac{\partial(\rho\boldsymbol{v})}{\partial t}+\nabla\cdot\left(\rho\boldsymbol{v}\boldsymbol{v}+\left(P+\frac{B^2}{2\mu_0}\right)\mathcal{I}-\frac{1}{\mu_0}\boldsymbol{B}\boldsymbol{B}\right)=0 \tag{15}$$

$$\frac{\partial e}{\partial t} + \nabla \cdot \left(\left(e + P + \frac{B^2}{2\mu_0} \right) \boldsymbol{v} - \frac{1}{\mu_0} \boldsymbol{B} (\boldsymbol{v} \cdot \boldsymbol{B}) \right) = 0 \tag{16}$$

$$\frac{\partial \boldsymbol{B}}{\partial t} + \nabla \cdot (\boldsymbol{B}\boldsymbol{v} - \boldsymbol{v}\boldsymbol{B}) = 0 \tag{17}$$

where,

$$e = \frac{P}{\gamma - 1} + \frac{1}{2}\rho v^2 + \frac{1}{2\mu_0} B^2. \tag{18}$$

2.2 Nondimensionalization

The MHD equations are nondimensionalized, with the primary purpose of eliminating the permeability of free space, μ_0, from the equations. This is done in order to allow the user to run calculations in MKS units and arrive at the same solution as they would had the calculation been run with units in which $\mu_0 = 1$, as is often the case in MHD studies. In MKS units, the user-defined initial magnetic field is normalized by $\sqrt{\mu_0}$ (eliminating μ_0 from Eqs. (15) – (16)), the pressure is normalized by 101325 Pa, density by 1 kg/m^3, length by 1 m, and temperature by 101325/R$_u$ K where R$_u$ is the universal gas constant. The normalizations for all other variables and constants are determined in relation to these five. The normalization for temperature was chosen such that molecular weight and specific heat ratio remain unchanged under normalization. In the remainder of this paper we will assume the normalized, nondimensional unit system and will therefore omit μ_0 from all equations.

2.3 DG formalism

Before presenting the DG discretization and specific numerical methods in Section 3, we formalize the derived ideal MHD equations here.

Let $\Omega \subset \mathbb{R}^d$ be a d-dimensional domain with boundary $\partial\Omega$, over which an outward normal $n : \partial\Omega \to \mathbb{R}^d$ is defined, and $T \subset \mathbb{R}^+$ is a given temporal interval. The ideal MHD equations, Eqs. (14) – (17), defined in strong form for piecewise smooth, $\mathbb{R}^m$-valued functions y, with gradient ∇y, are given as

$$\frac{\partial y}{\partial t} + \nabla \cdot \mathcal{F}(y) - \mathcal{S}(y, \nabla y) = 0 \text{ in } \Omega \times T, \tag{19}$$

$$y(\cdot, t_0) - y_0 = 0 \text{ in } \Omega, \tag{20}$$

$$n \cdot \mathcal{F}(y) - n \cdot \mathcal{F}_\partial(y) = 0 \text{ on } \partial\Omega \times T, \tag{21}$$

where t denotes time, $\mathcal{F} : \mathbb{R}^m \to \mathbb{R}^{m\times d}$ is a known convective flux function, and $\mathcal{S} : \mathbb{R}^m \to \mathbb{R}^m$ is a known source term that may be a function of the the gradient of the state. The initial conditions at time t_0 are given by y_0. The boundary conditions given by Eq. (21) are enforced through the boundary flux, $\mathcal{F}(y)$.

The ideal MHD flow state variable is given by

$$y = (\rho, \rho v_1, \rho v_2, \rho v_3, e, B_1, B_2, B_3), \tag{22}$$

where the velocity and magnetic field vectors, $\boldsymbol{v}$ and $\boldsymbol{B}$, always have three components, such that $m = 8$. The k-th spatial convective flux component is given by

$$\mathcal{F}_k(y) = \begin{pmatrix} \rho v_k \\ \rho v_1 v_k + P_t \delta_{k1} - B_k B_1 \\ \rho v_2 v_k + P_t \delta_{k2}, -B_k B_2 \\ \rho v_3 v_k + P_t \delta_{k3} - B_k B_3 \\ v_k(e + P_t) - B_k(\boldsymbol{v} \cdot \boldsymbol{B}) \\ v_k B_1 - v_1 B_k \\ v_k B_2 - v_2 B_k \\ v_k B_3 - v_3 B_k \end{pmatrix}, \tag{23}$$

where the total pressure, $P_t = P + B^2/(2\mu_0)$ is the sum of the fluid dynamic pressure and magnetic pressure.

3. FORMULATION

Assume the domain Ω is partitioned by $\mathcal{T}$, made up of discrete cells κ, with interfaces ϵ composing a set $\mathcal{E}$, over which an oriented normal $n : \epsilon \to \mathbb{R}^d$ is defined. Also assume that $\mathcal{E}$ consists of two disjoint subsets: the interior interfaces $\epsilon_{\mathcal{I}} \in \mathcal{E}_{\mathcal{I}}$ and the exterior interfaces $\epsilon_{\partial} \in \mathcal{E}_{\partial}$. For interior interfaces there exists $\kappa^+, \kappa^- \in \mathcal{T}$ such that $\epsilon_{\mathcal{I}} = \partial\kappa^+ \bigcap \partial\kappa^-$ and n^+, n^- are outward facing normals of κ^+, κ^-, respectively. Lastly, assume that there is a continuous invertible mapping, $u : \hat{\Omega} \to \Omega$, from reference domain $\hat{\Omega} \subset \mathbb{R}^d$ to the physical domain $\Omega \subset \mathbb{R}^d$.

Now, we use a discrete subspace V_h^p over $\mathcal{T}$ of piecewise polynomials. Let $\mathcal{P}_p$ be the space of polynomials spanned by the monomials $\boldsymbol{x}^\alpha$ with multi-index $\alpha \in \mathbb{N}_0^d$, satisfying $\alpha_i \leq p$ for $i = 1, ..., d$. Then,

$$V_h^p = \left\{ v \in \left[L^2(\Omega)\right]^m \middle| \forall \kappa \in \mathcal{T}, v|_\kappa \circ u \in \left[\mathcal{P}_p\right]^m \right\}. \tag{24}$$

3.1 Discretization

The DG (semi-)discretization of Eqs. (19) – (21) is defined as: find $\frac{\partial y}{\partial t} \in V_h^p$ such that

$$\sum_{\kappa\in\mathcal{T}} \left(\frac{\partial y}{\partial t}, v\right)_\kappa - \sum_{\kappa\in\mathcal{T}} (\mathcal{F}(y), \nabla v)_\kappa + \sum_{\epsilon\in\mathcal{E}} (h(y,n), [\![v]\!])_\mathcal{E} - \sum_{\kappa\in\mathcal{T}} (\mathcal{S}(y, \nabla y - L_0(y)), v)_\kappa = 0 \quad \forall v \in V_h^p \text{ and } \forall t \in T, \tag{25}$$

where $(\cdot,\cdot)$ denotes the inner product, $h(y,n)$ is the numerical flux, $[\![\cdot]\!]$ denotes the jump operator, and $L_0(y)$ is a global lifting operator. The discrete solution is given by the coefficients of a nodal basis defined for each element at the Guass-Lobatto points of that element. The volume and surface terms of Eq. (25) are numerically evaluated with a quadrature free method [7].

On interior interfaces, $\mathcal{E}_\mathcal{I}$, the jump and numerical flux terms are defined as

$$[v] = v^+ - v^- \text{ on } \epsilon \quad \forall \epsilon \in \mathcal{E}_\mathcal{I}, \tag{26}$$

$$h(y,n) = h(y^+, y^-, n) \text{ on } \epsilon \quad \forall \epsilon \in \mathcal{E}_\mathcal{I}. \tag{27}$$

On the exterior interfaces, $\mathcal{E}_\partial$, they are defined as

$$[v] = v^+ \text{ on } \epsilon \quad \forall \epsilon \in \mathcal{E}_\partial, \tag{28}$$

$$h(y,n) = h_\partial(y^+, n^+) \text{ on } \epsilon \quad \forall \epsilon \in \mathcal{E}_\partial, \tag{29}$$

where $h_\partial(y^+, n^+)$ is the numerical boundary flux. The only boundary conditions applied in this work are Dirichlet at an inflow with a fully assigned state, and Dirchlet at an outflow with the full state defined by the interior state, y^+. Any boundary without one of these two conditions is periodic and treated as an interior interface.

Equation (25) is integrated temporally with a second order strong-stability-preserving Runge-Kutta method, with a time step that is restricted by the Courant-Friedrichs-Lewy (CFL) number, defined as

$$\text{CFL} = \frac{\Delta t}{(2p+1)\min(\Delta x)} \lambda_{\max}, \tag{30}$$

where $\lambda_{\max}$ is the fastest wave speed (discussed below).

3.2 Numerical flux

Seven wave speeds characterize the ideal MHD equations and are defined as the eigenvalues of the flux jacobian of the system. These are two Alfvén waves, two fast magnetosonic waves, two slow magnetosonic waves, and one entropy wave defined as

$$\lambda_{2,6} = v \mp c_a,\ \lambda_{1,7} = v \mp c_f,\ \lambda_{3,5} = v \mp c_s,\ \lambda_4 = v, \tag{31}$$

respectively, where

$$c_a = \frac{|B_n|}{\sqrt{\rho}},\ c_{f,s} = \left(\frac{\gamma P + B^2 \pm \sqrt{\left(\gamma P + B^2\right)^2 - 4\gamma P B_n^2}}{2\rho} \right), \tag{32}$$

and the following is necessarily true:

$$\lambda_1 \leq \lambda_2 \leq \lambda_3 \leq \lambda_4 \leq \lambda_5 \leq \lambda_6 \leq \lambda_7. \tag{33}$$

The numerical flux $h(y^+, y^-, n)$ determined at each interior interface $\epsilon_{\mathcal{I}}$ must preserve stability and accuracy across potential discontinuities. We have implemented two different numerical fluxes that are commonly used with the ideal MHD system: a Rusanov flux [8], where

$$h(y^+, y^-, n) = \frac{1}{2}(\mathcal{F}(y^+) + \mathcal{F}(y^-)) - \frac{1}{2}|\lambda_{\max}|[y], \tag{34}$$

and a Roe flux [9], where

$$h(y^+, y^-, n) = \frac{1}{2}(\mathcal{F}(y^+) + \mathcal{F}(y^-)) - \frac{1}{2}\sum_i \boldsymbol{L_i}[y]|\lambda_i|\boldsymbol{R_i}. \tag{35}$$

λ_{max} represents the maximum wavespeed between the two states. This Rusanov flux is highly diffusive and less accurate because the dissipation term for every state variable scales by the maximum wave speed. In the Roe flux, the dissipation term is made up of the left and right eigenvectors, $\boldsymbol{L_i}$ and $\boldsymbol{R_i}$, of the flux jacobian of the Roe-averaged state. The complete eigensystem for ideal MHD can be found in the Athena code documentation [10]. This dissipation, scaled separately by each wave speed λ_i is much less diffusive than that of the Rusanov flux, making the Roe flux more accurate. For this reason we have used the Roe flux for all benchmarks in this work.

3.3 Divergence cleaning

Any MHD model must properly handle and enforce the magnetic divergence criterion; that is, the magnetic field should remain exactly or approximately divergence free through integration. While this holds in reality and is easily enforced in analytical contexts, in a simulation, even if the divergence is zero for the initial conditions, the nature of the numerical integration can cause an unphysical divergence to arise and threaten the accuracy and stability of a solution. There have been many proposed methods to deal with this fact [11].

Powell, et al. [12] established an 8-wave formulation of the ideal MHD equations. Instead of eliminating the divergence terms that arise in the derivation, these terms are included as source terms dependent on the divergence of the magnetic field:

$$\mathcal{S}_{\text{powell}}(y, \nabla y) = -\nabla \cdot \boldsymbol{B}(0, \boldsymbol{B}, \boldsymbol{u} \cdot \boldsymbol{B}, \boldsymbol{B}). \tag{36}$$

This has the affect of adding an eighth wave to the eigensystem of the ideal MHD equations that propagate at the local speed $\boldsymbol{v}$. Thus, any nonphysical divergence that arises convects with the fluid velocity as opposed to remaining in the same location and growing until triggering a numerical instability. These source terms have the additional attribute of making the MHD system Galilean invariant.

In the same vain of convecting divergence errors Dedner, et al. [13] developed a generalized Lagrange multiplier (GLM) formulation, in which a new scalar conservation equation is introduced for the Lagrange multiplier, ϕ. The multiplier is nonzero when a nonzero divergence is present and facilitates the advection of the magnetic divergence at a specific wave speed, c_h. Dedner, et al. also introduced a dissipating source term in the multiplier conservation equation, such that the divergence dissipates while it convects. This is a mixed hyperbolic-parabolic formulation of the Lagrange multiplier; therefore, we refer to it as the mixed GLM (MGLM) formulation. The flow state variable becomes

$$y = (\rho, \rho v_1, \rho v_2, \rho v_3, e, B_1, B_2, B_3, \phi), \tag{37}$$

and the flux and source terms are given as

$$\mathcal{F}_{\text{MGLM},k}(y) = \begin{pmatrix} \rho v_k \\ \rho v_1 v_k + P_t \delta_{k1} - B_k B_1 \\ \rho v_2 v_k + P_t \delta_{k2}, -B_k B_2 \\ \rho v_3 v_k + P_t \delta_{k3} - B_k B_3 \\ v_k (e + P_t) - B_k (\boldsymbol{v} \cdot \boldsymbol{B}) \\ v_k B_1 - v_1 B_k + \phi \delta_{k1} \\ v_k B_2 - v_2 B_k + \phi \delta_{k2} \\ v_k B_3 - v_3 B_k + \phi \delta_{k3} \\ c_h^2 B_k \end{pmatrix}, \quad \mathcal{S}_{\text{MGLM}}(y, \nabla y) = \begin{pmatrix} 0 \\ \mathbf{0} \\ 0 \\ \mathbf{0} \\ -\frac{c_h^2}{c_p^2} \phi \end{pmatrix}, \tag{38}$$

where c_p is a presribed value to control the amount of dissipation relative to the multiplier wave speed.

Lastly, Dedner, et al. extended the MGLM fomulation with energy and multiplier sources dependent on the gradient of ϕ, and made it Galilean invariant with the addition of the Powell source terms. We refer to this as the Galilean invariant extended GLM (GIEGLM), for which the source term becomes

$$\mathcal{S}_{\text{GIEGLM}}(y, \nabla y) = \begin{pmatrix} 0 \\ -(\nabla \cdot \boldsymbol{B})\boldsymbol{B} \\ -(\nabla \cdot \boldsymbol{B})\boldsymbol{v} \cdot \boldsymbol{B} - \boldsymbol{B} \cdot (\nabla \phi) \\ -(\nabla \cdot \boldsymbol{B})\boldsymbol{B} \\ -\boldsymbol{v} \cdot (\nabla \phi) - \frac{c_h^2}{c_p^2}\phi \end{pmatrix}. \tag{39}$$

The inclusion of the Powell source terms in the GIEGLM formulation splits Powell's eighth wave into two and gives it a velocity component, such that the new wave speeds are $v \pm c_h$. This is most desirable as a divergence cleaning scheme because the c_h component will convect divergence away from regions of zero velocity, such as stagnation points, and the velocity component prevents the advection of divergence upstream in a supersonic flow. The GLM and 8-wave formulations do not have both of these attributes, making GIEGLM the best cleaning scheme for all applications. All three schemes are implemented in the JENRE® Framework and we discuss in Section 4.5 their relative efficacy, then use GIEGLM for all subsequent cases.

As for the prescribed values in this formulation, Derigs, et al. [8] propose a spatially constant multiplier wave speed that is free to change each time step but restricted from exceeding the maximum wave speed, so as not to interfere with the CFL criterion determining the timestep size. This is given as

$$c_h = \lambda_{\max} - v_{\max,\Omega}, \tag{40}$$

where $v_{\max,\Omega} = \max_\Omega(|v_1|, |v_2|, |v_3|)$ is the greatest fluid speed in the domain. For the multiplier dissipation source term, both Dedner, et al. and Derigs, et al. prescribe c_p such that the ratio $c_r = c_p^2/c_h$ remains the same at all times. The optimal ratio, and the one we use here, was found to be $c_r = 0.18$.

3.4 Nonconservative source terms

For the nonconservative, gradient sources introduced in the previous section the source term discretization in Eq. (25) requires the global lifting operator [14],

$$L_0(y) = \sum_{\epsilon \in \mathcal{E}} L_0^\epsilon(y), \tag{41}$$

defined in terms of the local lifting operator,

$$(L_0^\epsilon(y),\tau)_\kappa = (\llbracket y \otimes n \rrbracket, \{\{\tau\}\})_\epsilon \quad \forall \tau \in \Sigma_h^p, \tag{42}$$

where $\{\{\cdot\}\}$ is the average operator and $\Sigma_h^p = \left[V_h^p\right]^2$ is the space of vector-valued discontinuous piecewise polynomial functions of degree $p \geq 0$ [15].

It was found during implementation and preliminary testing that the lifting operator was required in order to see the correct propagation of the magnetic divergence in the Powell and GIEGLM formulations. This is because the propagation wave speeds with a local velocity component are not dependent explicitly on the convective fluxes; rather, they are enforced and arise through the proper determination and integration of the divergence source terms.

3.5 Artificial viscosity

To stabilize oscillations that would arise at discontinuities, the local flux is augmented by a residual-based artificial viscosity used in [16] given as

$$\mathcal{F}^{\text{av}}(y,\nabla y) = \left((1 + S_{\text{av}}(p))\left(C_{\text{av}}\tilde{h}_k^2 \left|\frac{\partial T}{\partial y}\cdot\frac{\mathcal{R}(y,\nabla y)}{T}\right|\right)\right)\nabla y, \tag{43}$$

where $\tilde{h}_k = h_k/(p+1)$ and h_k is the characteristic length scale of the cell, $\mathcal{R}(y,\nabla y)$ is the strong form of the residual, Eq. (19), $\partial T/\partial y$ is the jacobian of the temperature with respect to the state variables, C_{av} is a user defined coefficient, and S_{av} is a pressure-dependent shock sensor that differentially weights where and how much aritificial viscosity is applied and is the same as that used by Ching et al. [17]. This shock-capturing technique proved to work well for our ideal MHD implementation.

4. RESULTS

Throughout the development process, many benchmark cases were used to check the implementation of the numerical flux, divergence cleaning, and shock-capturing. The most important and telling test cases are presented here.

4.1 Circularly-polarized Alfvén wave

An Alfvén wave is a rotational wave front with a propagation speed lying between that of fast and slow magnetosonic waves. A propagating Alfvén wave changes the direction, but not the magnitude, of the fluid velocity and magnetic field components perpendicular to the direction of wave propagation. There should be no change in fluid pressure, magnetic pressure, or density across the wave front. The circularly-polarized Alfvén wave is a smooth benchmark that is often used, in one, two, or three dimensions, to check MHD models because it has a simple analytical solution after every cycle of periodic wave propagation that corresponds precisely to the initial state. Here, we use a version used by Tóth [11] to look at the performance of the Roe flux in two dimensions.

The wave travels at an angle $\alpha = 30^o$ with respect to the x-direction with a unit wave length on a mesh with triangular elements, periodic boundaries, and spatial coordinates $0 < x < 1/\cos\alpha$ and $0 < y < 1/\sin\alpha$. The problem is initialized with $\rho = 1$, $P = 0.1$, $v_\perp = 0.1\sin(2\pi x_\parallel)$, $B_\perp = 0.1\sin(2\pi x_\parallel)$, and $V_z = B_z = 0.1\cos(2\pi x_\parallel)$ with $\gamma = 5/3$ where $\perp$ denotes vector components perpendicular to the direction of wave propagation and the spatial component parallel to the direction of wave propagation is given by $x_\parallel = x\cos\alpha + y\sin\alpha$. These initial conditions correspond to a wave speed that should return the wave profile to its initial state every unit of time $t = 1$.

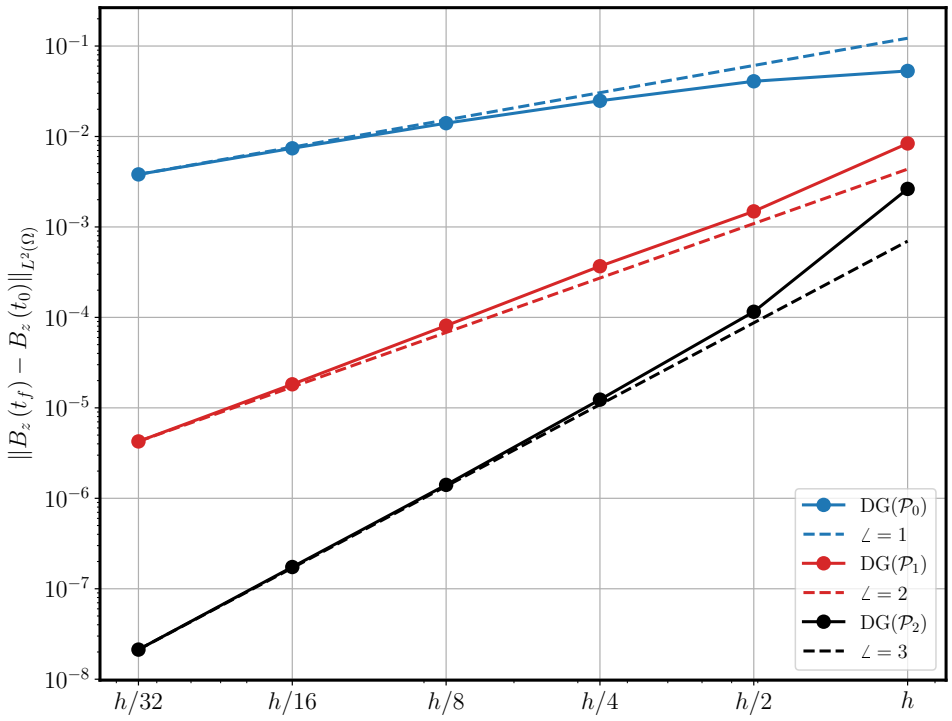

Fig. 1—2D Alfvén wave after 1 cycle, $t = 1$, showing convergence of B_z profile with h-refinement for different order elements

Figure 1 presents the L^2 errors in B_z after one cycle ($t = 1$), demonstrating the convergence of the numerical scheme for various spatial accuracies under mesh-(h-)refinement. The prescribed spatial accuracy is set by the polynomial order $\mathcal{P}$ and, should theoretically be of the order $2\mathcal{P} + 1$, assuming the temporal error is significantly smaller than the spatial. We set the CFL number to 0.1 for all cases, and assume this gives a small enough error with RK2 temporal integration. We have plotted the theoretical convergence with the computational results, showing good agreement. This sufficiently validates our implementation and use of the Roe numerical flux solver.

4.2 Shock tube

One-dimensional shock tube cases are frequently used [8, 9, 18, 19] in MHD to check the implementation of the shock-capturing method used as well as the ability of the model to capture the many wave speeds and discontinuities that can arise in an MHD system. For the validation of our shock sensor and artificial viscosity we use two of the most common MHD shock tube test cases: Ryu-Jones [19] and Brio-Wu [18].

4.2.1 Ryu-Jones shock tube

The initial states (left and right) for the Ryu-Jones shock tube are presented in Table 1. The 1D solution with $\mathcal{P}_1$ elements at time $t = 0.2$ is shown in Fig. 2 where each of the emerging discontinuities is labeled between the plots of density and B_y. From left to right these are a fast shock, rotational discontinuity, slow shock, contact discontinuity, slow shock, rotational discontinuity, and a fast shock. All of these represent one of the eigenvalues of the ideal MHD system and therefore a particular wave speed. In comparing the results with and without artificial viscosity, numerical oscillations (overshoots and undershoots) can be seen in the black line at every discontinuity. These oscillations are mitigated significantly when aritificial viscosity is applied locally at those steep gradients. Additionally, using a Roe flux with $\mathcal{P}_1$ elements produces crisp, well-resolved shocks in every case, validating our higher-order implementation.

Table 1—Initial left and right states for the Ryu-Jones shock tube

	ρ	P_f	v_x	v_y	v_z	B_x	B_y	B_z
left state	1.08	0.95	1.2	0.01	0.5	$2/\sqrt{4\pi}$	$3.6/\sqrt{4\pi}$	$2/\sqrt{4\pi}$
right state	1.0	1.0	0	0	0	$2/\sqrt{4\pi}$	$4/\sqrt{4\pi}$	$2/\sqrt{4\pi}$

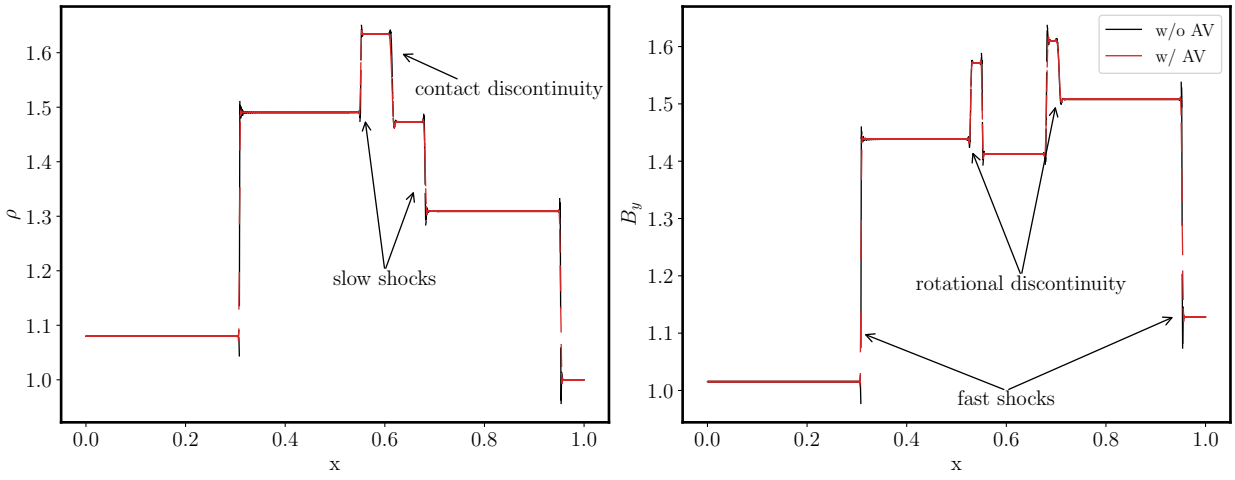

Fig. 2—(left) Density and (right) B_y at $t = 0.2$ of the 1D Ryu-Jones shock tube with $\mathcal{P}_1$ elements, demonstrating the effect of artificial viscosity (AV), with MHD waves labeled

4.2.2 Brio-Wu shock tube

The initial states (left and right) for the Brio-Wu shock tube are presented in Table 2. This shock tube benchmark is the same as the traditional sod shock tube problem for fluid dynamics [20] except a magnetic field is present, with a 180^o discontinuity in B_y at initialization. The 1D solution with $\mathcal{P}_1$ elements at time $t = 0.1$ is shown in Fig. 3 where the dramatic effect of the magnetic field's presence can be seen. From left to right the emergent waves in this case are a fast rarefaction, slow compound wave, contact discontinuity, slow shock, and another fast rarefaction. Without aritificial viscosity, the compound wave is completed inaccurately, producing two discrete jumps in density and magnetic field. The uniqueness of the compound wave that emerges once artificial viscosity is included makes this case an especially important test for an MHD solver.

Table 2—Initial left and right states for the Brio-Wu shock tube

	ρ	P_f	v_x	v_y	v_z	B_x	B_y	B_z
left state	1.0	1.0	0	0	0	0.75	1.0	0
right state	0.125	0.1	0	0	0	0.75	-1.0	0

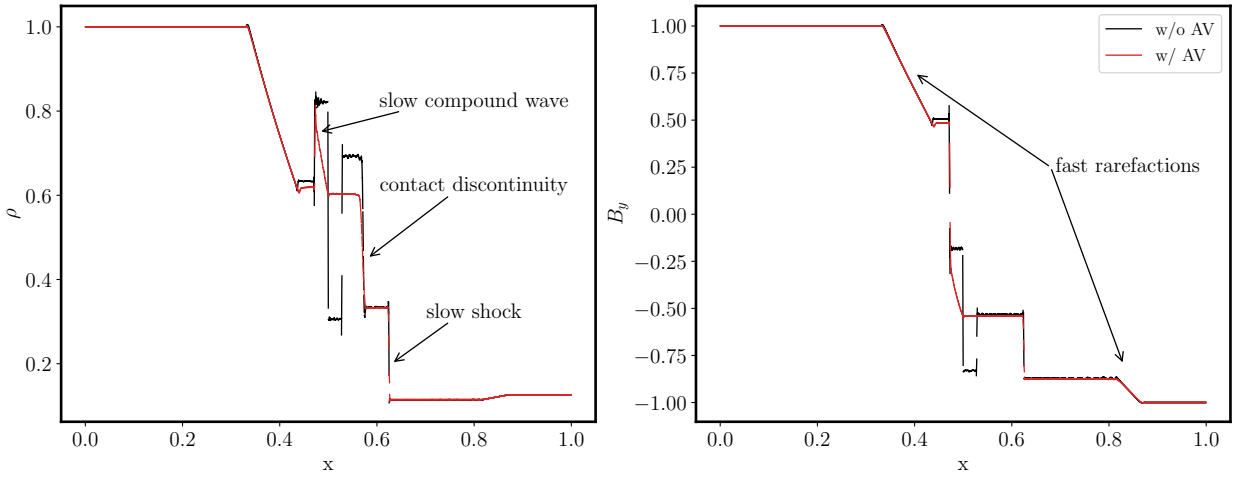

Fig. 3—(left) Density and (right) B_y at $t = 0.1$ of the 1D Brio-Wu shock tube with $\mathcal{P}_1$ elements, demonstrating the effect of artificial viscosity (AV), with MHD waves labeled

Given the success of the shock sensor and artificial viscosity demonstrated in these shock tube benchmarks, every subsequent test case presented here will be applying local artificial viscosity at the steep gradients to stabilize shock-laden flows.

4.3 Magnetized blast wave

The presence of a strong magnetic field in the region of a traditional blast wave has a large impact on its development and resulting dynamics due to the directional dependence of MHD wave speeds relative to the magnetic field. A magnetized, spherical blast wave is a common benchmark [10] for ideal MHD models because of the significant and predictable qualitative difference compared to an unmagnetized blast wave. With that said, we will first consider an unmagnetized blast wave's development, and then compare the results in a strong magnetic field.

The computational domain for this case is a periodic rectangle with $-0.5 < x < 0.5$ and $-0.75 < y < 0.75$ discretized into a 400x600 square element mesh. A high pressure circular region is initialized at the center with a radius of 0.1. The quiescent background gas has a density of 1, a fluid pressure of 0.1, and a γ of 5/3. The fluid pressure in the center is 10, giving a pressure ratio of 100. Figure 4(a) shows the density of the unmagnetized blast wave at time $t = 0.1$. As the blast wave propagates outward in a circle, the center becomes rarified, resulting in a low density region in the center and a gradient outward. While the unmagnetized blast wave provides a base case to compare the magnetized blast wave to, it also provides evidence that the numerical fluxes and general MHD implementation are correctly reducing to the Euler equations when there is no magnetic field present.

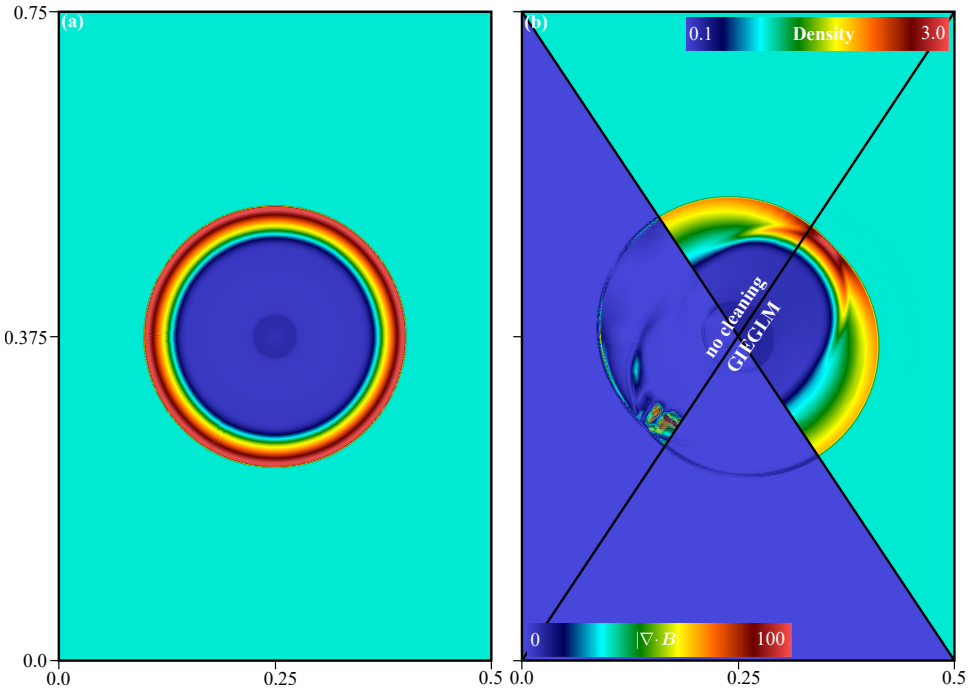

Fig. 4—(a) Density at $t = 0.1$ of the unmagnetized blast wave with $\mathcal{P}_1$ elements on a 400x600 mesh and (b) density and magnetic divergence of the magnetized blast wave with and without divergence cleaning.

We now initialize the same case with a constant magnetic field throughout the domain with a magnitude of 1 pointing along a 45^o angle. Figure 4(b) shows the result at time $t = 0.1$ and compares the results without divergence cleaning to those using the GIEGLM. First, we note that the presence of the magnetic field stretches the blast wave and resulting low density region in the center. This is because the fast magnetosonic wave travels faster perpendicular to the magnetic field than along it. The result is a more complex blast wave shape. Second, the case where cleaning is applied does, in fact, look cleaner, whereas without cleaning, there is noticeable graininess in the density plot from pile-up of unphysical magnetic divergence. This is seen in the bottom left portion of Fig. 4(b), as well, where we plot the local magnetic divergence for both cases.

Table 3—L^2-error of magnetic divergence for different cleaning methods, compared to no cleaning, in the magnetized blast wave

	no cleaning	Powell	MGLM	GIEGLM
$\|\nabla \cdot \boldsymbol{B}\|_2$	1.5102	2.8902	0.3832	0.3821
improvement	0%	-91%	75%	75%

Table 3 presents the L^2-error of magnetic divergence at $t = 0.1$ relative to the desired value of zero everywhere. We include the results for each of the three cleaning techniques discussed in Section 3.3. Compared to no cleaning, the MGLM and GIEGLM reduce the divergence error by 75%. Powell, on the other hand, produces greater error than when cleaning is not included and, in fact, produces a poor result overall that results in numerical instability. This is because the Powell source terms, while making the system Galilean invariant, also make it nonconservative, and in a case with strong shocks such as this the

nonphysical divergence arising immediately behind the shock wave is so great as to make the nonconservation destabilizing. While the GIEGLM contains these same source terms, it also contains the Lagrange multiplier and dissipates the divergence as it propagates, which is enough to retain numerical stability. Meanwhile, the comparable improvements of the MGLM and GIEGLM, and the fact that the latter convects the divergence with the fluid velocity, leads us to choose the GIEGLM as the preferred divergence cleaning method, as was stated in Section 3.3.

4.4 Magnetic rotor

The magnetic rotor is another 2D benchmark that produces shock waves in a strong magnetic field, thus testing our shock-capturing method and divergence cleaning technique. It models a dense, rotating fluid at the center of a square domain in a quiescent, magnetized background gas. We use a computational domain with $-0.5 < x, y < 0.5$ and a 512x512 triangular element mesh. The initial conditions are listed in Table 4. Rather than a sharp initial discontinuity we use smooth transitions in velocity and density from the dense rotating disk to the outer fluid at rest. The magnetic field is initially constant throughout the domain, pointing along the x-direction. As the center fluid rotates with its initially prescribed velocity the magnetic field wraps up with it. The interface between the dense disk and background gas is inherently unstable, and the coiling magnetic field launches Alfvén waves outward. This produces a low pressure, low density region in the center, where the dense disk once was.

Table 4—Initial conditions for the magnetic rotor where $f(r) = \frac{0.115-r}{0.115-0.1}$

	ρ	P_f	v_x	v_y	v_z	B_x	B_y	B_z
$r < 0.1$	10.0	1.0	$-20.0y$	$-20.0x$	0	$5/\sqrt{4\pi}$	0	0
$r \in (0.1, 0.115)$	$1.0 + 9.0f(r)$	1.0	$-20.0f(r)y$	$-20.0f(r)x$	0	$5/\sqrt{4\pi}$	0	0
$r < 0.115$	1.0	1.0	0	0	0	$5/\sqrt{4\pi}$	0	0

A snapshot at time $t = 0.295$ of the magnetic rotor is shown in Fig. 5. A compilation of four different images together visualizes the entirety of the comutational domain. We again compare the result without and with divergence cleaning, on the left and right side, respectively, and visualize fluid pressure on the top and the shock sensor on the bottom for each of the two cases. There is a clear difference in both pressure and shock sensor when divergence cleaning is not performed. The accumulation of magnetic divergence in certain regions produces the same grainy look where the soluton should be smooth. Moreover, looking at the bottom right of this figure, we can confirm that the shock sensor is working correctly, focusing only on regions of large gradient where artificial viscosity should be applied. When divergence cleaning is not included, it has an adverse effect, not just on the overall solution, but also on the efficacy of the shock sensor, making it overapply aritificial viscosity throughout smooth regions of the domain.

4.5 Orszag-Tang vortex

Another commonly used, shock laden benchmark for ideal MHD is the Orszag-Tang vortex, originally proposed by Orszag & Tang [21] to study small-scale MHD turbulence. It has become a standard for all ideal MHD solvers, testing shock formation and interaction, general MHD dynamics, divergence cleaning techniques, and the overall stability of the numerical solver. The domain is a square with sides of unit length and periodic boundary conditions. Initially the density is $25/(36\pi)$, the pressure is $5/(12\pi)$, and $\gamma = 5/3$, while $v_x = \sin(2\pi y)$, $v_y = \sin(2\pi x)$, $B_x = -B_0\sin(2\pi y)$, and $B_y = B_0\sin(4\pi x)$, where $B_0 = 1/\sqrt{4\pi}$.

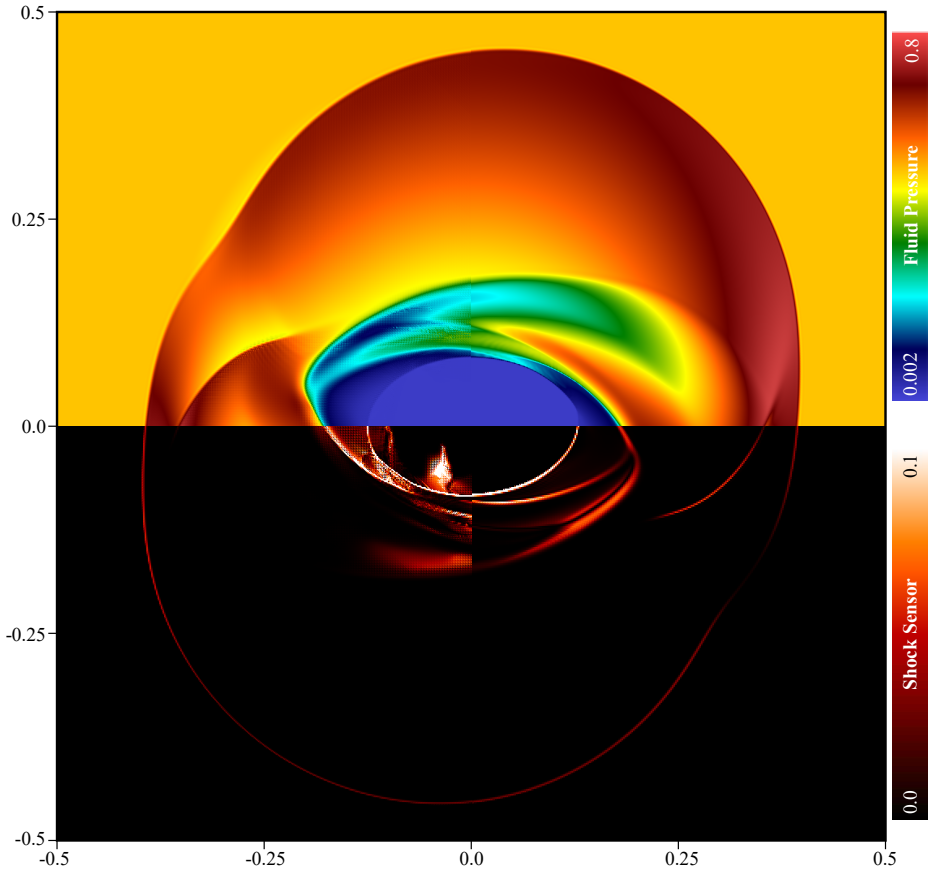

Fig. 5—(top) Fluid Pressure and (bottom) shock sensor for the magnetic rotor at $t = 0.295$ for $\mathcal{P}_1$ elements on a 512x512 mesh (left) without divergence cleaning and (right) with divergence cleaning

Figure 6 shows the result at time $t = 0.5$, on a triangular mesh that is 512x512 with $\mathcal{P}_1$ elements. A complex shock structure has emerged and a naturally forming current sheet in the center is beginning to generate magnetic islands. This is where a sharp gradient in the component of the magnetic field perpendicular to the gradient is present; in this case, the magnetic field is pointed to the right immediately below the centerline and pointed to the left above it. This means there is a large current density (current sheet) pointed into the page ($\boldsymbol{J} = \nabla \times \boldsymbol{B}$) which, under ideal MHD conditions, energetically recombines and forms magnetic islands. The left side of Fig. 6 shows this beginning to occur in the plasma density, and the right side shows the efficacy of the aritificial viscosity, being applied not only to strong shocks, but also to the regions of high current density. Moreover, the simulation has remained stable and divergence clean up to this point, and continues to do so through $t = 1.0$.

4.6 Current sheet

A current sheet, discussed briefly in the previous section, is where a sharp gradient is present in the component of the magnetic field perpendicular to that gradient, producing a large current density in the direction perpendicular to both. Under perturbations, the magnetic field reconnects across the current sheet and, without the presence of viscous effects, as in ideal MHD, this reconnection occurs through the formation of magnetic islands. Our final benchmark isolates this phenomenon. The domain is a square with sides of

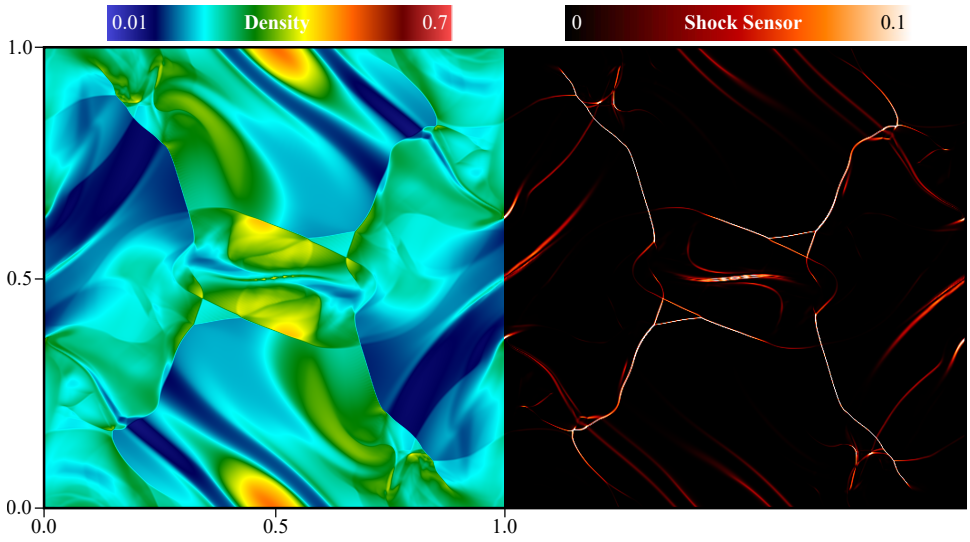

Fig. 6—(left) Density and (right) shock sensor for the Orszag-Tang vortex at $t = 0.5$ for $\mathcal{P}_1$ elements on a 512x512 mesh

unit length and periodic boundaries. The density is 1, the pressure is $\beta/2$, $\gamma = 5/3$, while $v_x = A\sin(2\pi y)$, $v_y = 0$, $B_y = -1$ for $0.25 \leq x \leq 0.75$ and $B_y = 1$ otherwise. For our test case, we use $\beta = 0.2$, $A = 0.2$.

Figure 7 shows B_y at time $t = 5$ for four different resolutions of $\mathcal{P}_1$ triangular elements. The sinusoidal perturbation in v_x induces the initial current sheets to shed Alfvén waves perpendicular to the current, in turn inducing more perturbation throughout the domain as the two current sheets reconnect by forming initially small magnetic islands. These islands convect up and down the current sheet and eventually collide and combine with other islands, forming larger ones. Not only does the detail of the magnetic islands improve with mesh refinement, but the positioning of the islands also converges to a something quite different than in the coarsest mesh. This emphasizes the importance of sufficient resolution in cases involving magnetic reconnection. This case also provides additional validation of the numerical flux solver, the divergence cleaning, and the robustness of the solver overall.

5. FUTURE WORK

With the goal of developing MHD modeling capabilities that can be used to study the interaction of hypersonic flows with electromagnetic fields, ideal MHD is the proper starting point but it does not go far enough in accounting for the physical phenomena that play a significant role in these systems. The partially ionized plasma that forms around hypersonic reentry and boost-glide vehicles have a magnetic Reynolds number much lower than is typically justifying of ideal MHD. That is, the magnetic field's convective flux, found in Eq. (23), is much smaller relative to the diffusive flux in these plasmas than in, for example, astrophysical contexts. In fact, an intentionally applied magnetic field at the nose cone of a reentry vehicle (either through a current-carrying solenoid or permanent magnets) may be diffusion dominated. The transport constant that arises in the MHD equations to account for the magnetic diffusion is the plasma resistivity. Thus the equations are deemed resistive MHD and are given by,

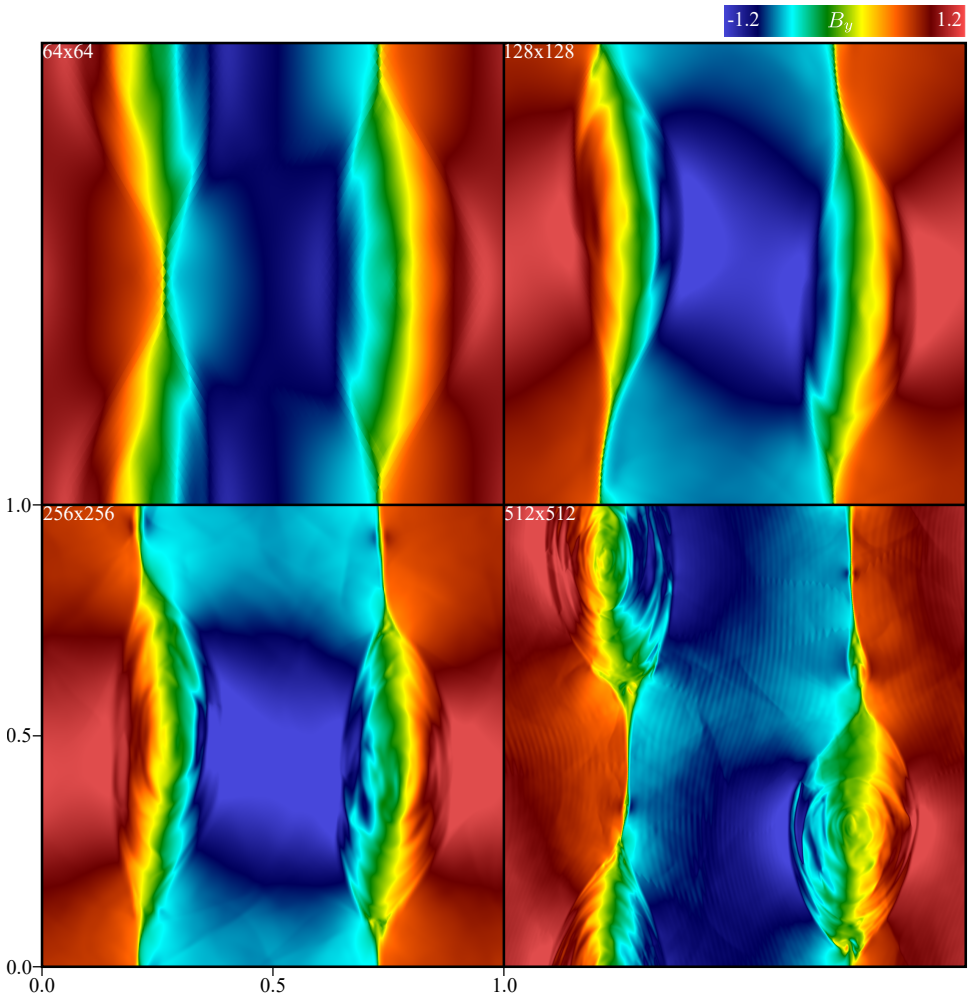

Fig. 7—The DG($\mathcal{P}_1$) approximate solution of the y-component of the magnetic field, B_y, at time $t = 5$ on a sequence of uniformly refined triangular grids

$$\frac{\partial}{\partial t}\begin{pmatrix}\rho\\ \rho\boldsymbol{v}\\ e\\ \boldsymbol{B}\\ \phi\end{pmatrix}+\nabla\cdot\begin{pmatrix}\rho\boldsymbol{v}\\ \rho\boldsymbol{v}\boldsymbol{v}+(P_f+\frac{1}{2}|\boldsymbol{B}|^2)\mathcal{I}-\boldsymbol{B}\boldsymbol{B}\\ \boldsymbol{v}(e+P_f+\frac{1}{2}|\boldsymbol{B}|^2)-\boldsymbol{B}(\boldsymbol{v}\cdot\boldsymbol{B})\\ \boldsymbol{v}\boldsymbol{B}-\boldsymbol{B}\boldsymbol{v}+\phi\mathcal{I}\\ c_h^2\boldsymbol{B}\end{pmatrix}$$
$$-\nabla\cdot\begin{pmatrix}\boldsymbol{0}\\ \boldsymbol{\tau}\\ \boldsymbol{\tau}\cdot\boldsymbol{v}+\kappa\nabla T-\eta\boldsymbol{B}\cdot\left((\nabla\boldsymbol{B})^{\mathrm{T}}-\nabla\boldsymbol{B}\right)\\ \eta\left((\nabla\boldsymbol{B})^{\mathrm{T}}-\nabla\boldsymbol{B}\right)\\ \boldsymbol{0}\end{pmatrix}=\begin{pmatrix}0\\ -(\nabla\cdot\boldsymbol{B})\boldsymbol{B}\\ -\boldsymbol{B}\cdot\nabla\phi\\ \boldsymbol{0}\\ -\frac{c_h^2}{c_p^2}\phi\end{pmatrix}, \tag{44}$$

where the EGLM formulation is still included for divergence cleaning. Here, the viscous stress tensor is defined as,

$$\boldsymbol{\tau} = \mu \left((\nabla \boldsymbol{v})^{\mathrm{T}} + \nabla \boldsymbol{v} - \frac{2}{3} \nabla \cdot \boldsymbol{v} \bar{\mathcal{I}} \right), \tag{45}$$

where μ is the dynamic viscosity.

The second of the two flux terms on the LHS of Eq. (44) is the viscous flux, which accounts for three diffusive transport phenomena in the fluid: viscosity, thermal conductivity, and resistivity. With these transport constants properly chosen, the MHD benchmarks and dynamics considered in this paper can change significiantly. The implementation of resistive MHD in the JENRE® Code, that is the addition of the viscous fluxes, is the next step that will be taken towards development of a robust and accurate plasma-dynamics solver for the study of electromagnetic interaction with hypersonic flows.

6. CONCLUSIONS

In this paper we motivated the development of a coupled electromagnetic-fluid dynamic solver for the multidisciplinary field of hypersonics, and presented the initial steps taken to achieve this. We outlined the existing numerical model and solvers present in NRL's JENRE® Multiphysics Framework, and described the MHD capabilities that have been developed. The natural starting point has been implementing a solver for the ideal MHD equations, which are an idealized coupling of the inviscid Euler equations with Maxwell's electromagnetic equations.

Although the application of an ideal MHD solver to a hypersonics context is limited, we have outlined through multiple benchmark cases the capabilities that have been developed thus far that lay the groundwork for modeling more realistic plasma dynamics and interactions. These main developments are (1) the implementation of an accurate Roe-type numerical flux for MHD, (2) the inclusion and demonstration of a magnetic divergence cleaning method that is well-defined for DG numerical solvers, and (3) the effective implementation of a shock sensor for local application of artificial viscosity for the MHD solver, in particular. The latter development has been crucial in modeling these benchmark cases with high-order spatial accuracy, and it will play an important role going forward in producing and trusting well-resolved numerical results down the line.

Lastly, we have addressed a plan of action going forward, which is to include viscous fluxes in the existing MHD solver to account for magnetic resistivity and possible diffusion-dominated flows in the hypersonic regime. The implementation of resistive MHD will be followed by an evaluation of its efficacy in modeling the hypersonic systems that we are interested in. A multiple-temperature or multiple-species model may need to be pursued for certain specific plasma applications, such as plasma-assisted combustion. Regardless, the essential tools for MHD and plasma modeling in complex geometries are now at the disposal of NRL and will be developed and used extensively going forward.

ACKNOWLEDGMENTS

This work was made possible through the Karle's Fellowship Program at the U.S. Naval Research Laboratory.

REFERENCES

1. K. M. Hanquist, H. Alkandry, and I. D. Boyd, "Evaluation of computational modeling of electron transpiration cooling at high enthalpies," *Journal of Thermophysics and Heat Transfer* **31**(2), 283–293 (2017).

2. M. Kundrapu, J. Loverich, K. Beckwith, P. Stoltz, A. Shashurin, and M. Keidar, "Modeling radio communication blackout and blackout mitigation in hypersonic vehicles," *Journal of Spacecraft and Rockets* **52**(3), 853–862 (2015).

3. Y. X. Sha, H. L. Zhang, X. Y. Guo, and M. Y. Xia, "Analyses of electromagnetic properties of a hypersonic object with plasma sheath," *IEEE Transactions on Antennas and Propagation* **67**(4), 2470–2481 (2019).

4. W. L. Jones and A. E. Cross, *Electrostatic-probe measurements of plasma parameters for two reentry flight experiments at 25000 feet per second*, volume 6617 (National Aeronautics and Space Administration, 1972).

5. R. L. Kimmel, D. Adamczak, D. Hartley, H. Alesi, M. A. Frost, R. Pietsch, J. Shannon, and T. Silvester, "HIFiRE-5b flight overview," Proceedings of the 47th AIAA Fluid Dynamics Conference, 2017, p. 3131.

6. P. Mocz, M. Vogelsberger, D. Sijacki, R. Pakmor, and L. Hernquist, "A discontinuous Galerkin method for solving the fluid and magnetohydrodynamic equations in astrophysical simulations," *Monthly Notices of the Royal Astronomical Society* **437**(1), 397–414 (2014).

7. H. L. Atkins and C. W. Shu, "Quadrature-free implementation of discontinuous Galerkin method for hyperbolic equations," *AIAA journal* **36**(5), 775–782 (1998).

8. D. Derigs, A. R. Winters, G. J. Gassner, S. Walch, and M. Bohm, "Ideal GLM-MHD: About the entropy consistent nine-wave magnetic field divergence diminishing ideal magnetohydrodynamics equations," *Journal of Computational Physics* **364**, 420–467 (2018).

9. P. Cargo and G. Gallice, "Roe matrices for ideal MHD and systematic construction of Roe matrices for systems of conservation laws," *Journal of Computational Physics* **136**(2), 446–466 (1997).

10. J. M. Stone, T. A. Gardiner, P. Teuben, J. F. Hawley, and J. B. Simon, "Athena: a new code for astrophysical MHD," *The Astrophysical Journal Supplement Series* **178**(1), 137 (2008).

11. G. Tóth, "The$\nabla\cdot$ B= 0 constraint in shock-capturing magnetohydrodynamics codes," *Journal of Computational Physics* **161**(2), 605–652 (2000).

12. K. G. Powell, P. L. Roe, T. J. Linde, T. I. Gombosi, and D. L. De Zeeuw, "A solution-adaptive upwind scheme for ideal magnetohydrodynamics," *Journal of Computational Physics* **154**(2), 284–309 (1999).

13. A. Dedner, F. Kemm, D. Kröner, C. D. Munz, T. Schnitzer, and M. Wesenberg, "Hyperbolic divergence cleaning for the MHD equations," *Journal of Computational Physics* **175**(2), 645–673 (2002).

14. F. Bassi, F. Cecchi, N. Franchina, S. Rebay, and M. Savini, "High-order discontinuous Galerkin computation of axisymmetric transonic flows in safety relief valves," *Computers & fluids* **49**(1), 203–213 (2011).

15. R. Hartmann and T. Leicht, "Higher order and adaptive DG methods for compressible flows," *37th Advanced CFD Lecture Series: Recent developments in higher order methods and industrial application in aeronautics* **2014**(3), 1–156 (2014).

16. R. F. Johnson and A. D. Kercher, "A conservative discontinuous Galerkin discretization for the chemically reacting Navier-Stokes equations," *Journal of Computational Physics* **423**, 109826 (2020).

17. E. J. Ching, Y. Lv, P. Gnoffo, M. Barnhardt, and M. Ihme, "Shock capturing for discontinuous Galerkin methods with application to predicting heat transfer in hypersonic flows," *Journal of Computational Physics* **376**, 54–75 (2019).

18. M. Brio and C. C. Wu, "An upwind differencing scheme for the equations of ideal magnetohydrodynamics," *Journal of computational physics* **75**(2), 400–422 (1988).

19. D. Ryu and T. Jones, "Numerical magnetohydrodynamics in astrophysics: algorithm and tests for one-dimensional flow," *The Astrophysical Journal* (1995).

20. G. A. Sod, "A survey of several finite difference methods for systems of nonlinear hyperbolic conservation laws," *Journal of computational physics* **27**(1), 1–31 (1978).

21. S. A. Orszag and C. M. Tang, "Small-scale structure of two-dimensional magnetohydrodynamic turbulence," *Journal of Fluid Mechanics* **90**(1), 129–143 (1979).